

DOI: 10.1002/celec.201402041



Interplay between Nitrogen Concentration, Structure, Morphology, and Electrochemical Performance of PdCoNi “Core–Shell” Carbon Nitride Electrocatalysts for the Oxygen Reduction Reaction

Enrico Negro,^[a, b] Keti Vezzù,^[c] Federico Bertasi,^[a, b] Piero Schiavuta,^[c] Luigi Toniolo,^[b, d] Stefano Polizzi,^[b, d] and Vito Di Noto^{*[a, b]}

This report describes the electrochemical behavior of a family of “core-shell” electrocatalysts consisting of a carbon nitride (CN) “shell” matrix and a “core” of conducting carbon nanoparticles (NPs). The CN “shell” matrix embeds PdCoNi alloy NPs and covers homogeneously the carbon “core”. The chemical composition of the materials is determined by inductively-coupled plasma atomic emission spectroscopy (ICP-AES) and microanalysis; the structure is studied by powder X-ray diffraction (powder XRD); the morphology is investigated by high-resolution transmission electron microscopy (HR-TEM). The surface activity and structure are probed by CO stripping. The oxygen reduction reaction (ORR) kinetics, reaction mechanism, and tolerance towards contamination from chloride anions are evalu-

ated by cyclic voltammetry with the thin-film rotating ring-disk electrode (CV-TF-RRDE) method. The effect of N concentration in the matrix (which forms “coordination nests” for the Pd-based alloy NPs bearing the active sites) on the ORR performance of the electrocatalysts is described. Results show that N atoms: 1) influence the evolution of the structure of the materials during the preparation processes, and 2) interact with alloy NPs, affecting the bifunctional and electronic ORR mechanisms of active sites and the adsorption/desorption processes of oxygen molecules and contaminants. Finally, the best PdCoNi electrocatalyst shows a higher surface activity in the ORR at 0.9 V vs. RHE with respect to the Pt-based reference ($388 \mu\text{A cm}_{\text{Pd}}^{-2}$ vs. $153 \mu\text{A cm}_{\text{Pt}}^{-2}$).

1. Introduction

The development of affordable energy-conversion systems characterized by a high efficiency and a low environmental impact is one of the most important challenges faced by both fundamental and applied science. Many solutions have been proposed, ranging from advanced secondary batteries based on alkaline- and alkaline-earth elements, to supercapacitors and redox flow batteries.^[1–3] One additional family of energy conversion systems that complies with the above requirements

includes the various types of fuel cells (FCs), which are open devices that are able to convert the chemical energy obtained from the oxidation of a fuel (usually hydrogen or small organic molecules such as methanol, formic acid or methane) directly into electrical energy.^[4]

In particular, proton-exchange membrane fuel cells (PEMFCs) arouse significant interest because of their high conversion efficiency and power density; such systems are suitable for a variety of applications ranging from portable electronics to light-duty vehicles.^[5] The operation of PEMFCs is bottlenecked by the sluggishness of the oxygen reduction reaction (ORR) in the highly acid environment generated by the electrolyte.^[6] Suitable electrocatalysts must be mounted in the device to achieve a performance level compatible with applications. Thus, the development of efficient and affordable ORR electrocatalysts is one of the most critical goals of the research in the field of PEMFCs.^[7,8]

Today's state of the art in ORR electrocatalysts for application in PEMFCs consists of nanocomposite materials including Pt nanocrystals supported on conductive carbon nanoparticles.^[7] These electrocatalysts yield an acceptable performance but require a significant loading of platinum, whose abundance in Earth's crust is very limited and is expected to raise significant risks of supply bottlenecks.^[9,10] Furthermore, Pt-based electrocatalysts show a relatively poor tolerance to common contaminants such as halides and methanol.^[11,12]

[a] Dr. E. Negro, Dr. F. Bertasi, Prof. V. Di Noto
Department of Chemical Sciences
University of Padova
Via Marzolo 1, 35131 Padova (PD) (Italy)
E-mail: vito.dinoto@unipd.it

[b] Dr. E. Negro, Dr. F. Bertasi, Prof. L. Toniolo, Prof. S. Polizzi, Prof. V. Di Noto
Consorzio Interuniversitario Nazionale
per la Scienza e la Tecnologia dei Materiali
INSTM (Italy)

[c] Dr. K. Vezzù, Dr. P. Schiavuta
Veneto Nanotech S.C.p.a.
Via San Crispino 106, I-35129 Padova (PD) (Italy)

[d] Prof. L. Toniolo, Prof. S. Polizzi
Department of Molecular Sciences and Nanosystems
University of Venice
Calle Larga S. Marta, Dorsoduro
2137-30123 Venezia (VE) (Italy)

 Supporting Information for this article is available on the WWW under <http://dx.doi.org/10.1002/celec.201402041>.

 This manuscript is part of a Special Section devoted to the GEI 2013.

Indeed, it is well-known that the electrochemical behavior of platinum-group metal (PGM) surfaces is strongly affected by anion adsorption.^[13–16] In particular, chloride anions may contaminate the air supply of PEMFCs that operate on or near the sea, or that power vehicles running on roads where common deicing agents such as CaCl₂ are disseminated.^[12] One way to address the issues raised above is to investigate ORR electrocatalysts including Pd-based active sites.^[17] Palladium is more abundant than platinum in the Earth's crust; furthermore, it is possible to prepare Pd-based ORR electrocatalysts that are characterized by a good performance and a high tolerance to methanol contamination.^[17–19] It was also demonstrated that the introduction of nitrogen in the carbon matrix, giving rise to a carbon nitride matrix, has a crucial effect on the performance, structure, and tolerance to contaminants of Pd-based ORR electrocatalysts.^[20,21]

An innovative approach is adopted for the preparation of the Pd-based ORR electrocatalysts studied in this work.^[21,22] The method consists of the pyrolysis of a three-dimensional hybrid inorganic–organic precursor including clusters of metal coordination complexes embedding the desired metal atoms, which are bridged together through a suitable organic binder.^[21,22] The hybrid inorganic–organic precursor impregnates a support (the “core”) constituted by conducting carbon nanoparticles. After the pyrolysis process, the support is covered by a carbon nitride (CN) “shell” matrix, which is mainly derived from pyrolysis of the organic binder of the starting hybrid inorganic–organic precursor. Thus, the electrocatalysts obtained as the products of the pyrolysis process are characterized by a “core-shell” morphology, which yields significant improvements to the performance of the materials.^[23] The CN “shell” matrix embeds metal nanoparticles (NPs) based on Pd alloyed with Co and Ni, which bear the ORR active sites. These alloy NPs are bonded in “nitrogen coordination nests” of the CN “shell” matrix.^[20,24–26] The structure of the electrocatalysts is studied by powder XRD; the morphology is elucidated by HR-TEM. Indeed, it is well-known that the size, distribution, and structural features of NPs play an important role in the catalytic processes.^[27,28] Co and Ni are introduced as co-catalysts because it was demonstrated that they present the capability to boost the ORR performance of active sites based on PGMs (e.g. Pt and Pd).^[17,29] In this report, the effect of the introduction of a different binder in the synthesis of the precursor of the electrocatalysts is investigated. Consequently, a very different networking of the metal clusters is obtained in the precursor.^[21] At the same time, the stoichiometry of the metals is kept constant for all the investigated samples. Thus, two precursors have been synthesized, each comprising a different binder. The first precursor uses sucrose, and includes a low concentration of nitrogen. The second precursor employs polyacrylonitrile (PAN); accordingly its wt% of N is expected to be much higher. Two pyrolysis temperatures, T_f , are adopted for each precursor, 600 and 900 °C. Correspondingly, four distinct electrocatalysts are obtained, which are labeled as discussed henceforth:^[29] PdCoNi-CN_h 600/G, PdCoNi-CN_h 900/G, PdCoNi-CN_l 600/G, and PdCoNi-CN_l 900/G. In this report, the interplay between the preparation parameters (e.g. concentration of N

in the “shell” matrix and T_f), the structure, the morphology, the electrochemical performance in the ORR, and the tolerance to chloride anions of the electrocatalysts is elucidated. This study has been conducted within the framework of a continuing effort to obtain improved functional materials for application at the cathodes of PEMFCs.

2. Results and Discussion

2.1. Chemical Analysis

The chemical composition of the PdCoNi-CN_x T_f /G electrocatalysts is reported in Table 1. It was observed that all the materials include roughly the same wt% of metals and they were characterized by a metal stoichiometry that was very close to

Table 1. Chemical composition of the electrocatalysts.^[21]

Electrocatalyst	Weight [%]						Formula
	Pd ^[a]	Co ^[a]	Ni ^[a]	K ^[a]	C ^[b]	N ^[b]	
PdCoNi-CN _h 600/G	9.27	5.04	5.14	–	59.29	8.44	PdCo _{0.98} Ni _{1.0} C ₅₇ N _{6.9}
PdCoNi-CN _h 900/G	8.75	5.77	5.77	–	57.58	1.94	PdCo _{1.19} Ni _{1.20} C ₅₈ N _{1.7}
PdCoNi-CN _l 600/G	5.64	3.93	3.96	1.79	70.90	2.90	K _{0.87} [PdCo _{1.26} Ni _{1.27} C ₁₁₁ N _{3.9}]
PdCoNi-CN _l 900/G	6.64	4.71	4.51	0.82	71.40	0.78	K _{0.34} [PdCo _{1.28} Ni _{1.23} C ₉₅ N _{0.89}]

^[a] Determined by ICP-AES. ^[b] Determined by microanalysis.

the nominal values. A small wt% of K was detected in all the samples. This is a common feature of the products obtained with the preparation procedure adopted in this work.^[21] Furthermore, the wt% of N with respect to PdCoNi-CN_l T_f /G electrocatalysts 1) was higher in PdCoNi-CN_h T_f /G systems, and 2) decreased as T_f was raised from 600 to 900 °C. These features are in line with the results reported elsewhere and are a further proof of the good control of the stoichiometry that is achieved with the preparation protocol adopted in this work.^[21]

2.2. Structural Studies

The powder XRD spectra of the PdCoNi-CN_x T_f /G electrocatalysts were simulated by the Rietveld method to single out the types and characteristics of alloy NPs in the samples and to obtain a semiquantitative evaluation of their main figures of merit, such as their relative abundance, cell constants, and particle size.^[30] The corresponding information is summarized in Table 2.

Results obtained for the Pt/C reference are reported elsewhere.^[23] The complete attributions of the reflections (angular positions, interplanar distances, relative intensities and Miller indexing of alloy NPs) are provided in Table S1–S4 of the Supporting Information. Figure 1 shows the Rietveld simulation of the selected powder XRD spectrum of the PdCoNi-CN_l 900/G electrocatalyst. The analyses of the remaining PdCoNi-CN_x T_f /G

Table 2. Main parameters describing the phases identified by Rietveld analysis of the XRD patterns of the PdCoNi-CN_x T_f/G electrocatalysts.

PdCoNi-CN _h 600/G					
Phase	Co + Ni [%]	Space group	Wt %	Cell parameters [Å]	Particle size [nm]
Pd ₇₅ (CoNi) ₂₅ ^[a]	25	Fm-3m	8.13	a = 3.799	15.5
Pd ₆₁ (CoNi) ₃₉ ^[a]	39	Fm-3m	9.82	a = 3.747	10.6
Pd ₁₈ (CoNi) ₈₂ ^[a]	82	Fm-3m	1.31	a = 3.585	6.4
C	-	Fmmm	80.7	a = 2.46, b = 4.27, c = 7.12	2.3
PdCoNi-CN _h 900/G					
Pd ₅₀ (CoNi) ₅₀ ^[a]	50	Fm-3m	13.16	a = 3.705	26
Pd ₃₇ (CoNi) ₆₃ ^[a]	63	Fm-3m	7.40	a = 3.656	19
C	-	Fmmm	79.44	a = 2.47, b = 4.27, c = 7.00	2.2
PdCoNi-CN _i 600/G					
Pd ₉₁ (CoNi) ₉ ^[a]	9	Fm-3m	0.86	a = 3.859	14
Pd ₅₁ (CoNi) ₄₉ ^[a]	49	Fm-3m	7.85	a = 3.708	52
Pd ₁₂ (CoNi) ₈₈ ^[a]	88	Fm-3m	0.40	a = 3.563	27
Pd ₃ (CoNi)	24	Pm-3m	1.24	a = 3.806	42
C	-	Fmmm	89.6	a = 2.46, b = 4.27, c = 7.19	1.9
PdCoNi-CN _i 900/G					
Pd ₅₂ (CoNi) ₄₈ ^[a]	48	Fm-3m	11.39	a = 3.712	10.9
Pd ₃₄ (CoNi) ₆₆ ^[a]	66	Fm-3m	2.63	a = 3.645	50
Pd ₂₆ (CoNi) ₇₄ ^[a]	74	Fm-3m	2.25	a = 3.615	52
C	-	Fmmm	83.7	a = 2.46, b = 4.27, c = 7.15	3.8

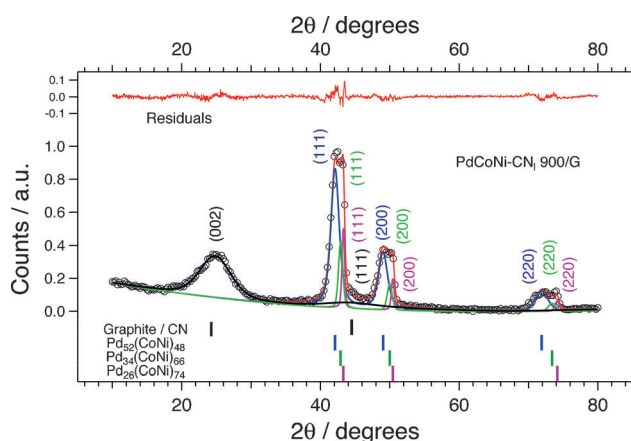


Figure 1. Results of the powder XRD pattern decomposition by the Rietveld procedure of the PdCoNi-CN_i 900/G electrocatalyst.

samples are reported in Figure S1–S3 of the Supporting Information.

In detail, the PdCoNi-CN_x T_f/G electrocatalysts present a clear peak at $2\theta \approx 25^\circ$, attributed to the (002) reflection of the carbon “core” support, comprising mostly the XC-72R nanoparticles. In accordance with results reported elsewhere,^[23] the particle size of ordered domains of the carbon “core” support is on the order of 2–4 nm for all the investigated electrocatalysts. The peaks at $2\theta \approx 45^\circ$ of the carbon “core” NPs show a low relative intensity (see Table S1–S4 of the Supporting Information) and are completely overlapped by the other reflections of the XRD patterns, which are ascribed to PdCoNi alloy

NPs with sharper and more intense peaks (see Figure 1 and Figure S1–S3 of the Supporting Information) located at $2\theta \approx 42^\circ$, 48° and 71° . These latter intensities were analyzed by the Rietveld procedure by using two or three different phases for alloy NPs, which are characterized by the same Fm-3m space group and by a different cell constant (see Table 2). The results are in accordance with reported data^[31,32] and show that palladium metal, which is characterized by the Fm-3m space group,^[33] easily forms alloys with Ni and Co metals. With respect to pristine Pd, Pd-M alloy NPs exhibit a similar structure with a decreasing cell constant as the concentration of the first-row transition metal M is raised.^[34,35] In conclusion, PdCoNi-CN_x T_f/G electrocatalysts exhibit more than one type of Pd-M alloy NPs, each characterized by a different concentration of the first-row transition metal M. The alloying behavior of Co and Ni towards Pd NPs is very similar. Thus, it is very difficult to distinguish the distribution of Co and Ni in Pd-M alloy NPs by powder XRD. Consequently, for simplicity, here the composition of the Pd-M alloy NPs is indicated as: Pd_{100-x}(CoNi)_x, where x is the alloying degree, i.e. the percentage of lattice sites in the Pd structure which has undergone substitution by either Co or Ni. PdCoNi-CN_i 600/G evidences a set of sharp peaks at $2\theta \approx 23.5^\circ$, 33.4° , 41.2° , 47.9° , 54.0° , 59.6° , 70.0° and 74.95° (see Table S1 and Figure S1 in the Supporting Information). These reflections are attributed to Pd₃(CoNi) NPs in a Pm-3m space group, which is isostructural with Cu₃Au NPs.^[36] In this case, the first-row transition metal atoms (M) have a regular periodic distribution among the sites of NPs, giving rise to a superlattice.^[36] In Pd-M alloy NPs, the first-row transition-metal atoms, M, are randomly distributed among the available lattice sites of NPs. Table 2 highlights the finding that as T_f is increased from 600 to 900 °C, the concentration of first-row transition metals in the PdCoNi alloys increases. This result is consistent with that of other electrocatalysts.^[24,37] As the temperature of the pyrolysis process T_f is raised, the diffusion of first-row transition metals from the carbon nitride-based “shell” matrix to the PGM-based alloy nanoparticles is increased,^[24,37] thus decreasing the number of distinct palladium-based phases. This evidence is interpreted as an indication that during the pyrolysis process at T_f = 900 °C the metal atoms acquire enough energy to rearrange, yielding alloy NPs characterized by a lower Gibbs free energy. In detail, the Pd₃(CoNi) NPs present in PdCoNi-CN_i 600/G disappear in PdCoNi-CN_i 900/G as the Ni and Co atoms become randomly distributed among the available lattice sites in the alloy domains, with a corresponding increase in configuration entropy. Furthermore, the Pd₁₈(CoNi)₈₂ phase, detected in PdCoNi-CN_h 600/G, is no longer present in PdCoNi-CN_h 900/G because its small nanocrystals (d = 6.4 nm) are merged into the other NPs with larger sizes (d = 26 and 19 nm) according to Ostwald ripening processes. Finally, with respect to PdCoNi-CN_h T_f/G electrocatalysts (d ≤ 26 nm), PdCoNi-CN_i T_f/G materials include larger PdCoNi alloy NPs with sizes up to d ≈ 50 nm. This result is attributed to the larger concentration of N atoms in the carbon nitride “shell” matrix of PdCoNi-CN_h T_f/G electrocatalysts. In detail, N atoms are expected to bind the PdCoNi alloy NPs in “N coordination nests”.^[20,24–26] These latter processes inhibit the diffusion of

metal atoms in the matrix and consequently restrain the growth processes of alloy NPs. The overall distribution of the alloy NPs phases identified in the PdCoNi-CN_x T_f/G electrocatalysts is coherent with the results of the chemical analysis reported in Table 1.

2.3. Morphology Studies

The TEM images referring to the PdCoNi-CN_x T_f/G electrocatalysts are shown in Figure 2. The results of the TEM investigation were consistent with the discussion on the structure of

alloy NPs are characterized by a particle size of approximately 60 nm; in contrast, the results of the Rietveld analysis reported in Table 2 indicate that the dominant Pd₅₂(CoNi)₄₈ phase is characterized by an average particle size distribution of approximately 11 nm. Thus, it is concluded that a significant fraction of the “large” PdCoNi grains of PdCoNi-CN₁ 900/G is polycrystalline. Figure 2e and f demonstrate that the proposed electrocatalysts are characterized by a “core-shell” morphology, in which a “core” of carbon conducting nanoparticles is homogeneously covered by a carbon nitride “shell” matrix embedding PdCoNi alloy NPs.

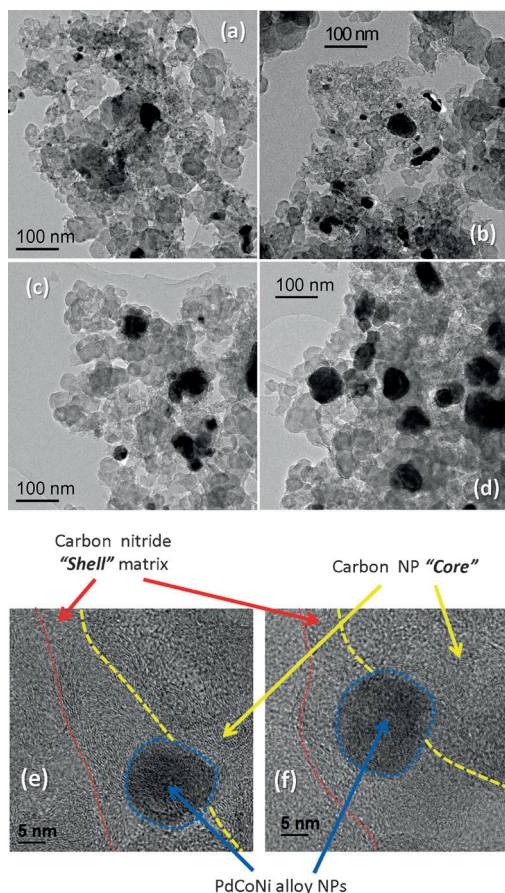


Figure 2. Morphology of the proposed PdCoNi-CN_x T_f/G electrocatalysts as determined by high-resolution transmission electron microscopy (HR-TEM). a) PdCoNi-CN_h 600/G; b) PdCoNi-CN_h 900/G; c) PdCoNi-CN_l 600/G; d) PdCoNi-CN_l 900/G. High-magnification micrographs evidencing the “core-shell” morphology of the proposed electrocatalysts: e) PdCoNi-CN_h 900/G and f) PdCoNi-CN_l 900/G.

the materials reported in Section 2.2, and with the results of the Rietveld analysis included in Table 2. With respect to PdCoNi-CN_h T_f/G electrocatalysts, the particle size of the PdCoNi alloy NPs of PdCoNi-CN_l T_f/G is larger by a factor of approximately 1.5 (see Figure 2a and b and Figure 2c and d, respectively). As an example, in PdCoNi-CN_h 600/G, the average size distribution of the “small” and “large” PdCoNi alloy NPs is approximately 10 and 40 nm, respectively. In PdCoNi-CN_l 600/G, the corresponding figures are approximately 14 and 60 nm, respectively. Inspection of Figure 2d reveals that most PdCoNi

2.4. Investigation of the Surface Structure by CO Stripping

The surface structure of PdCoNi-CN_x T_f/G electrocatalysts was investigated by CO stripping. This technique is particularly suitable for the study of materials including PGMs such as Pt, Pd, and others.^[38] CO stripping yields accurate information both on well-defined surfaces in experiments carried out on single crystals and on nanoparticles.^[39,40] Figure 3 reports the CO stripping currents obtained for the PdCoNi-CN_x T_f/G electrocatalysts and the Pt/C reference.

Additional information on the CO stripping profiles is reported in Figure S4 and Table S5 of the Supporting Information. As a general trend, the CO stripping events taking place on the PdCoNi-CN_x T_f/G electrocatalysts occur at a higher potential in comparison with the Pt/C reference. This result is rationalized by considering that CO molecules are oxidized to CO₂ upon stripping.^[40] In this process, CO must react with oxygen atoms

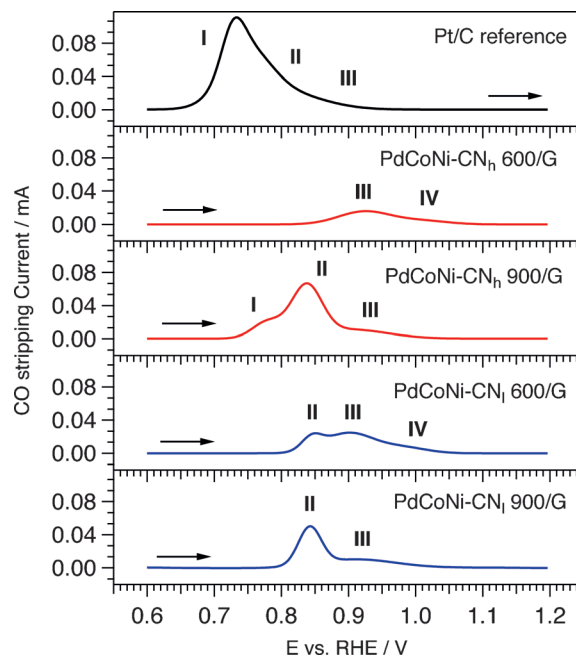


Figure 3. CO stripping currents of the proposed electrocatalysts and of the Pt/C reference. All the electrodes have a Pt/Pd loading of 15 μg cm⁻². Labels I, II, III, and IV indicate the detected CO stripping events. Cell filled with a 0.1 M HClO₄ solution, CO stripping sweep rate = 20 mV s⁻¹; the electrode tip was not rotated during CO stripping; P_{N₂} = 1 atm; the other experimental details are the same as those reported elsewhere.^[41]

adsorbed on the surface. Consequently, as the strength of the interactions between adsorbed oxygen atoms and the surface increases, the CO stripping potential is raised. Indeed, with respect to the Pt/C reference, all the PdCoNi-CN_x T_f/G electrocatalysts have a higher affinity towards oxygen, in accordance with the “harder” character of Pd in comparison to Pt.^[42] The main CO stripping event (III, see Figure 3) detected on PdCoNi-CN_x 600/G electrocatalysts is approximately 60–70 mV higher than with the main CO stripping event II characterizing the PdCoNi-CN_x 900/G materials. PdCoNi-CN_h 900/G evidences an additional CO stripping event I, at a potential lower by approximately 60 mV with respect to event II. These results are interpreted as follows. In the alloys between PGMs (e.g. Pt and Pd) and first-row transition metals M (e.g. Ni and Co), the contraction of the cell constant with respect to the unalloyed PGM gives rise to weaker interactions between the alloy surface and the oxygen adsorbates owing to an electronic mechanism.^[35] Consequently, the oxidation of CO molecules adsorbed on the metal atoms present on the surface of the alloy is facilitated and CO is stripped at a lower potential in comparison with the unalloyed PGM.^[41] In Section 2.2 it is demonstrated that as T_f is raised from 600 to 900 °C, the alloying degree x in the PdCoNi NPs increases. In a first approximation, this explains why the main stripping event II in PdCoNi-CN_x 900/G materials is located approximately 60–70 mV lower in comparison with the main stripping event III in PdCoNi-CN_x 600/G systems. Several other factors affect the CO stripping profiles, including the crystal face and the presence of contaminants on the PGM surfaces.^[43] The resulting picture is quite complex, and it becomes very hard to describe in detail all the different contributions to the CO stripping profiles. Nevertheless, a tentative correlation between the structure of the materials as determined by powder XRD and the features of the CO stripping profiles can be proposed. In PdCoNi-CN_i 600/G, the lightly alloyed phases Pd₉₁(CoNi)₉ and Pd₃(CoNi) are expected to collectively originate the two events III and IV, which are located at a relatively high potential (E > 0.9 V vs. RHE). Event II is attributed to the highly alloyed Pd₅₁(CoNi)₄₉ phase. The abundance of the latter phase is significantly higher in comparison with the Pd₉₁(CoNi)₉ and Pd₃(CoNi) phases (see Table 2). However, the particle size of Pd₅₁(CoNi)₄₉ is also the largest (d = 52 vs. 14 nm of Pd₉₁(CoNi)₉); correspondingly, a low surface area is expected, yielding a relatively small CO stripping event. In PdCoNi-CN_i 900/G, the main CO stripping event II is ascribed to the Pd₅₂(CoNi)₄₈ phase. The other phases (i.e. Pd₃₄(CoNi)₆₆ and Pd₂₆(CoNi)₇₄) are characterized by a low abundance and a large particle size (d ≈ 50 nm); thus, they provide a negligible contribution to the CO stripping profiles. In PdCoNi-CN_h 600/G, the stripping events III and IV are attributed to the lightly alloyed phase Pd₇₅(CoNi)₂₅, similar to the PdCoNi-CN_i 600/G electrocatalyst. The contributions of the more heavily alloyed phases (i.e. Pd₆₁(CoNi)₃₉ and Pd₁₈(CoNi)₈₂) to the CO stripping profiles are probably low, despite the significant abundance and the small particle sizes (d < 11 nm). This assumption is justified considering that the PdCoNi alloy NPs are nucleated in the CN “shell” matrix.^[21,23] Furthermore, the concentration of N in the PdCoNi-CN_h 600/G electrocatalyst is the highest (ca. 8.4%). As a result, most of

the Pd atoms are likely coordinated by the heteroatoms of the carbon nitride “shell”, with a particular reference to the N of the “coordination nests”. Thus, only a small concentration of Pd atoms is available to adsorb CO molecules and contribute to the stripping events. These phenomena are particularly pronounced for the Pd₆₁(CoNi)₃₉ and Pd₁₈(CoNi)₈₂ phases, which are characterized by a low concentration of Pd atoms, and by a small particle size, giving rise to a high surface concentration of highly reactive edge and corner sites in which heteroatom coordination is facilitated. This picture is also supported by TEM analysis, which shows small (d < 11 nm), highly alloyed PdCoNi NPs embedded in the CN “shell” matrix of PdCoNi-CN_h 600/G (see Figure S5 of the Supporting Information). In PdCoNi-CN_h 900/G, the main CO stripping event II is ascribed to the Pd₅₀(CoNi)₅₀ phase, similar to the PdCoNi-CN_i 900/G material. The stripping event I is assigned to the phase Pd₃₇(CoNi)₆₃; the high alloying degree yields a CO stripping peak centered at the lowest potential (E = 0.779 V vs. RHE). With respect to PdCoNi-CN_h 600/G, the wt% of nitrogen in PdCoNi-CN_h 900/G is significantly lower (ca. 1.9 vs. ca. 8.4%; see Table 1); furthermore, the particle size of the PdCoNi phases is relatively large (d = 26, 19 nm). Consequently, it is expected that a high fraction of Pd atoms are not coordinated by heteroatoms and are available to adsorb CO. A detailed assignment of the CO stripping events on the surface of the Pt/C reference is outside of the scope of this work. However, the overall shape of the CO stripping profile is similar to that reported elsewhere, pointing to the typical surface structure of platinum nanoparticles.^[39,40,44,45] The results of CO stripping measurements can be used to determine the electrochemical surface area (ECSA) of electrocatalysts characterized by active sites based on PGMs; the procedure involves integration of the overall CO stripping charge.^[39,40] The specific charge value used in this work is 484 μC cm_{Pd}⁻². This figure was chosen in accordance with previously reported PGM nanoparticles, from which it was deduced that the values of specific charge to be adopted for Pt- and Pd-based system match.^[35,39,45] The results are reported in Table 3.

Whereas the ECSA of PdCoNi-CN_i 600/G was larger than that of PdCoNi-CN_h 600/G, the opposite trend was recorded at T_f = 900 (see Table 3). The ECSA value of the Pt/C reference was 36.6 m² g_{Pt}⁻¹, in line with values reported elsewhere.^[46] These results are rationalized by considering that the Pd-based active sites on the surface of the alloy NPs can be fixed on the carbon nitride matrix upon coordination of nitrogen nests on the “shell”. It is expected that the active sites of PdCoNi-CN_h T_f/G and PdCoNi-CN_i T_f/G electrocatalysts are mainly blocked

Table 3. Figures of merit of the ORR performance of the proposed electrocatalysts.

Electrocatalyst	A _{Pt,Pd} [m ² g _{Pt,Pd} ⁻¹]	i _{m(0.9 V)} [A mg _{Pt,Pd} ⁻¹]	i _{s(0.9 V)} [μA cm _{Pt,Pd} ⁻²]
PdCoNi-CN _h 600/G	6.8	0.00143	21
PdCoNi-CN _h 900/G	21.6	0.0287	132
PdCoNi-CN _i 600/G	11.9	0.00717	60
PdCoNi-CN _i 900/G	11.9	0.0470	388
Pt/C reference	36.6	0.0563	153

by nitrogen- and carbon-based species, respectively. This picture is consistent with the chemistries of the hybrid inorganic-organic precursors of the two families of electrocatalysts. PdCoNi-CN_h T_f/G are obtained from the pyrolysis of a precursor with a relatively low proportion of nitrogen atoms (originally present as cyanometalates) and a sucrose binder.^[47] In contrast, PdCoNi-CN_h T_f/G electrocatalysts derive from a precursor characterized by a large weight concentration of nitrogen atoms, mainly provided by the polyacrylonitrile (PAN) macromolecules used as the binder.^[47] The sucrose binder is decomposed relatively easily during the pyrolysis process, leading to PdCoNi-CN_h 600/G, leaving behind a very porous conducting “shell” matrix distributed over the XC-72R “core” NPs. This behavior is typical of these electrocatalysts,^[21] and originates from the large concentration of oxygen and hydrogen atoms included in the sucrose binder. In contrast, decomposition of the PAN binder is expected to yield a much more compact matrix, featuring extensive “coordination nests” that are rich in nitrogen atoms around the PdCoNi alloy NPs.^[20,24–26] Consequently, at T_f=600 °C, a larger fraction of palladium-based active sites are available in PdCoNi-CN_h 600/G in comparison with PdCoNi-CN_h 900/G, resulting in a higher ECSA. It was anticipated that decomposition of the sucrose binder of the hybrid inorganic-organic precursor is likely complete at T_f=600 °C,^[21,24] therefore, little additional removal of blocking contaminants occurs for PdCoNi-CN_h 900/G. However, the overall ECSA is not increased because this effect is compensated for by the decrease in the surface area of PdCoNi alloy NPs triggered by the thermally-induced particle growth process (see Table 2). Nevertheless, the fraction of nitrogen atoms removed during the pyrolysis process of the precursor increases significantly as T_f is raised from 600 to 900 °C, as witnessed by the chemical composition of the PdCoNi-CN_x T_f/G electrocatalysts (see Table 1). As a consequence, in the hypothesis that the heteroatoms coordinating the Pd-based active sites in alloy NPs of the “shell” matrix of PdCoNi-CN_h T_f/G electrocatalysts are mostly nitrogen-based, the number of available ORR active sites in PdCoNi-CN_h 900/G is significantly larger in comparison with PdCoNi-CN_h 600/G. The overall result is that ECSA increases, because this effect is more important with respect to the decrease in surface area arising from the thermally-induced growth process.

2.5. ORR Performance and Reaction Mechanism of the Proposed Electrocatalysts

Figure 4 shows the profiles obtained by cyclic voltammetry with a thin-film rotating ring-disk electrode (CV-TF-RRDE) of the proposed electrocatalysts. Disk current densities are a measure of the performance in the ORR. Ring currents are used in the determination of the ORR selectivity in the “direct”, four-electron mechanism yielding water as the final product.^[41,48]

The fraction of hydrogen peroxide ($X_{\text{H}_2\text{O}_2}$) as a function of the applied potential is evaluated with Equation (1).^[11,41]

$$X_{\text{H}_2\text{O}_2} = \frac{\frac{2I_r}{N}}{I_D + \frac{I_r}{N}} \quad (1)$$

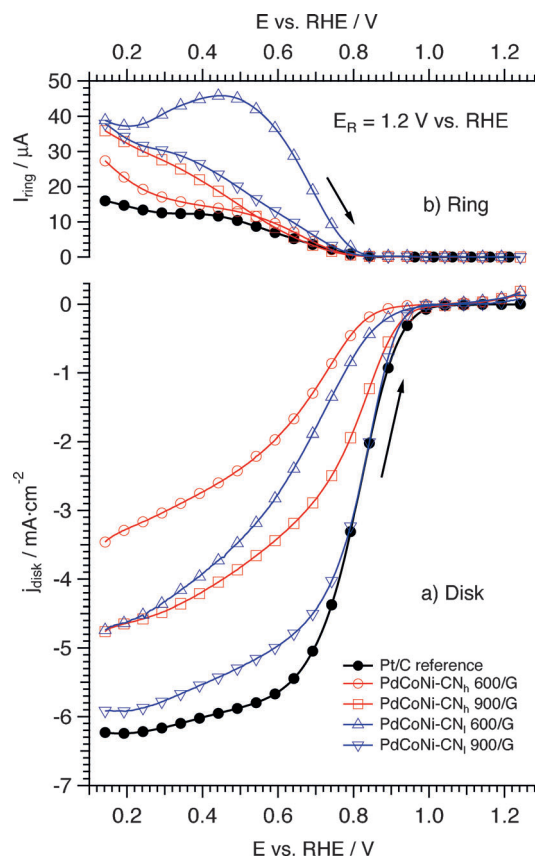


Figure 4. Positive-going sweeps of the Pt/C reference and of the prepared electrocatalysts in a pure-oxygen atmosphere. a) Current densities measured on a glassy-carbon disk; b) oxidation currents determined on a platinum ring. Cell filled with a 0.1 M HClO₄ solution, T = 60 °C, sweep rate = 5 mV s⁻¹, electrode rotation rate 1600 rpm, and PO₂ = 1 atm.

where I_D and I_R are the current detected on the glassy-carbon disk and the platinum ring, respectively; $N=0.38$ is the collection efficiency of the platinum ring. The results are reported in Figure 5.

All the proposed electrocatalysts are characterized by a remarkable ORR performance, which is significantly affected by

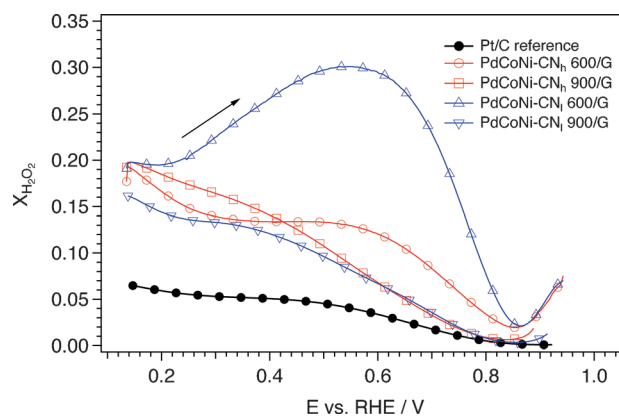


Figure 5. Fraction of hydrogen peroxide developed during the ORR on the PdCoNi-CN_x T_f/G electrocatalysts, determined with Equation (1). Results obtained from the traces shown in Figure 4.

the concentration of nitrogen and by T_f . Tests performed on samples based on a CN matrix not containing metals showed no contribution of the carbon nitride matrix to the ORR performance, in accordance with previous reports.^[49] As a general trend, the ORR performance increases as T_f is raised from 600 to 900 °C, and as the weight concentration of nitrogen is decreased. Inspection of the results reported in Figure 5 indicates clearly that, with respect to the Pt/C reference, all the proposed PdCoNi-CN_x T_f /G electrocatalysts are significantly less selective in the four-electron ORR mechanism, which is consistent with previous reports on other Pd-based systems.^[50] The poorest selectivity was recorded for PdCoNi-CN₁ 600/G, whereas the other three materials showed similar performance. These results are rationalized by considering that PGMs may carry out the ORR with the four-electron mechanism only in the presence of two neighboring sites that are free of adsorbates.^[23,48] Considering that palladium and platinum belong to the fifth and sixth period, respectively, the former element shows a higher affinity towards oxygen, leading to a more extensive covering with oxygen-based adsorbates.^[21] Thus, with respect to the Pt/C reference, a lower surface concentration of couples of neighboring active sites free of adsorbates is expected for the PdCoNi-CN_x T_f /G electrocatalysts, yielding an inferior ORR selectivity in the four-electron mechanism (see Figure 5). The ORR performance is evaluated as follows. The ORR faradic current densities are obtained from the curves shown in Figure 4 after the contributions arising from mass transport are removed with the usual expression valid for the RDE setup and reported below as Equation (2):^[51]

$$\frac{1}{j} = \frac{1}{j_k} + \frac{1}{j_d} \quad (2)$$

where j is the current density detected on the glassy-carbon disk, j_k is the faradic ORR current density, and j_d is the diffusion-limited current density. In this work, for each electrocatalyst j_d is set equal to the value assumed by the ORR trace shown in Figure 4 at a potential equal to 0.140 V vs. RHE. The faradic current density j_k obtained from Equation (2) is multiplied by the geometric area of the glassy carbon disk ($A = 0.196 \text{ cm}^2$), yielding i_k . The latter is normalized either on the total mass of PGMs on each electrode, that is, 2.95 μg , or on the total PGM surface area present on each electrode, evaluated by multiplying the ESCA values reported in Table 3 by the total mass of PGM on each electrode. The resulting two figures are the mass activity i_m and the surface activity i_s .^[46] The results are plotted in a semilogarithmic scale ("Tafel plots") in Figure 6a and b, respectively.

One way to gauge the performance of the proposed electrocatalysts in the ORR is to consider the values of i_m and i_s at 0.9 V vs. RHE, which are summarized in Table 3. The values of $i_{m(0.9 \text{ V})}$ of the PdCoNi-CN_x T_f /G electrocatalysts increase as the wt% of nitrogen decreases from PdCoNi-CN_h T_f /G to PdCoNi-CN_l T_f /G systems, and as T_f is increased from 600 to 900 °C. The maximum $i_{m(0.9 \text{ V})}$ is observed for PdCoNi-CN_l 900/G, with a value of 0.047 $\text{A mg}_{\text{Pd}}^{-1}$, which is only slightly lower than the

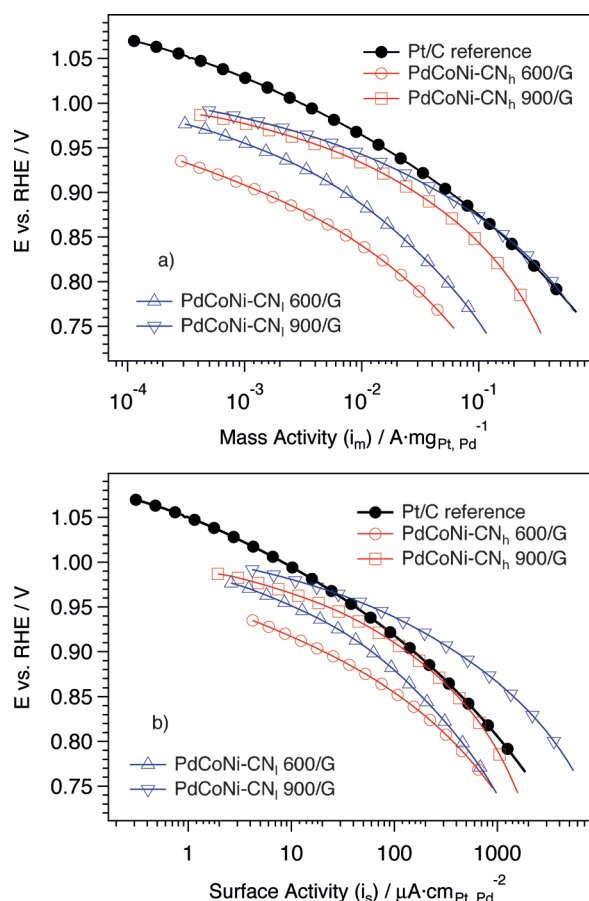


Figure 6. Tafel plots of the PdCoNi-CN_x T_f /G electrocatalysts and of the Pt/C reference. Profiles obtained from the traces reported in Figure 4 after removing the contributions arising from mass transport phenomena. a) Currents normalized on the mass of Pt/Pd on the electrode; b) currents normalized on the ECSA of the active sites evaluated from the data reported in Figure 3.

value of 0.0563 $\text{A mg}_{\text{Pt}}^{-1}$ for the Pt/C reference. The general trend observed for the values of $i_{s(0.9 \text{ V})}$ closely matches that characterizing $i_{m(0.9 \text{ V})}$. The main difference is that the maximum $i_{s(0.9 \text{ V})}$ value, shown by PdCoNi-CN_l 900/G (388 $\mu\text{A cm}_{\text{Pd}}^{-2}$), exceeds by a factor of approximately 2.5 that of the Pt/C reference (153 $\mu\text{A cm}_{\text{Pd}}^{-2}$). Inspection of Table 3 shows that for both PdCoNi-CN_h T_f /G and PdCoNi-CN_l T_f /G, $i_{s(0.9 \text{ V})}$ increases by a factor of approximately 6 as T_f is raised from 600 to 900 °C. Furthermore $i_{s(0.9 \text{ V})}$ increases by a factor of approximately 3 from PdCoNi-CN_h T_f /G to PdCoNi-CN_l T_f /G electrocatalysts at a given T_f (either 600 or 900 °C). The Tafel slopes of the traces reported in Figure 6 provide information concerning the ORR reaction mechanism.^[20,25] The Tafel slopes decrease as the ORR overpotential is reduced owing to progressive increase in the coverage of the active sites caused by oxygen-based adsorbates.^[20,25] All the proposed electrocatalysts and the Pt/C reference follow this general trend. The results summarized above can be rationalized in a coherent picture by taking into account the information obtained from the structure, the morphology, and the surface features of the electrocatalysts. The systematic six-fold increase in $i_{s(0.9 \text{ V})}$ observed as T_f is raised is justified as follows. Analysis of the powder XRD patterns (see

Section 2.2) provides evidence that the alloying degree x of the $\text{Pd}_{100-x}(\text{CoNi})_x$ phases present in the electrocatalysts rises as T_f is increased from 600 to 900 °C. Correspondingly, the cell constant becomes smaller and an electronic effect takes place, shifting to lower overpotentials the blocking of the ORR active sites by oxygen adsorbates.^[35] The observed three-fold increase in $i_{s(0.9\text{V})}$ both at $T_f=600$ °C and at $T_f=900$ °C from PdCoNi-CN_h T_f/G to PdCoNi-CN_l T_f/G is ascribed to a better incorporation of first-row transition metals (i.e. Co and Ni) in the active sites of the latter family of electrocatalysts. Co and Ni are known to act as co-catalytic elements in this family of carbon nitride electrocatalysts; since they are good Lewis acids, they promote the protonation of the ORR oxygen-based intermediates, allowing faster desorption of the products from the active sites according to a bifunctional mechanism. The result is a reduced ORR overpotential.^[21] The larger concentration of strongly adsorbed nitrogen atoms in PdCoNi-CN_h T_f/G in comparison with PdCoNi-CN_l T_f/G is expected to deactivate this mechanism, as witnessed by similar results reported elsewhere.^[20,25,26]

2.6. Effect of Poisoning by Chloride Anions on the ORR Performance

The PdCoNi-CN_x T_f/G electrocatalysts and the Pt/C reference were tested in the ORR in the presence of a progressively increasing concentration of Cl^- anions (10^{-4} , 10^{-3} , and 10^{-2} mol·dm⁻³); the results are shown in the Supporting Information. The data were analyzed by using the procedure discussed in Section 2.5. In detail, $X_{\text{H}_2\text{O}_2}$ is determined with Equation (1) starting from the traces reported in the Supporting Information; the results are summarized in Figure 7.

Tafel plots in the ORR were also determined and are shown in Figure 8 for the Pt/C reference, PdCoNi-CN_h T_f/G , and PdCoNi-CN_l T_f/G electrocatalysts.

The potential difference between the curves corresponding to $[\text{Cl}^-]=0$ and those collected at an increasing concentration of chloride anions are displayed in Figure 9.

The reported values were determined at $\log_{10}(\text{current density})=-1$. This latter value was chosen because it is small enough to require only small corrections (lower than ca. 5%) to compensate mass transport effects, and because it is large enough to limit uncertainties arising from the removal of capacitive currents. Inspection of Figure 7 allows to conclude that the ORR selectivity in the four-electron mechanism of both the proposed electrocatalysts and of the Pt/C reference is decreased in the presence of chloride anion contaminations. This effect increases in the order Pt/C reference < PdCoNi-CN_h T_f/G < PdCoNi-CN_l T_f/G . One additional outcome of the increase in $[\text{Cl}^-]$ is the slower ORR kinetics, which is reflected in the increasing ORR overpotential, as shown in Figure 8 and Figure 9. In particular, Figure 9 reveals that the ORR overpotential increases the most for PdCoNi-CN_l T_f/G electrocatalysts, whereas the effect on both the Pt/C reference and PdCoNi-CN_h T_f/G is similar. These experimental results are rationalized by comparing the fundamental interactions between the active sites of the Pt/C reference and the PdCoNi-CN_x T_f/G electrocatalysts, and between the nitrogen, oxygen, and chloride spe-

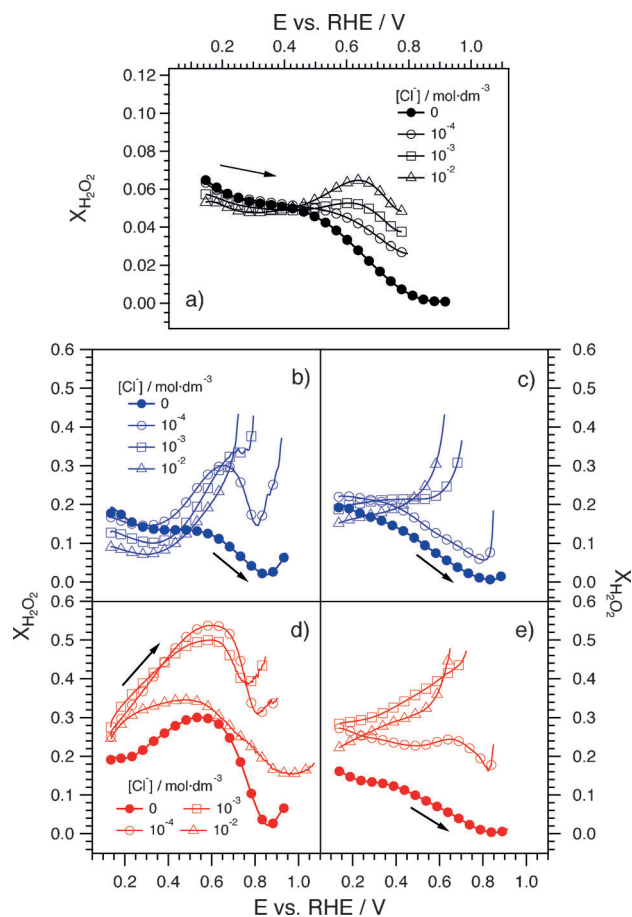


Figure 7. Dependence on chloride anion concentration $[\text{Cl}^-]$ of the fraction of H_2O_2 produced in the ORR by the PdCoNi-CN_x T_f/G electrocatalysts and the Pt/C reference, determined with Equation (1) starting from the traces reported in the Supporting Information. a) Pt/C reference; b) PdCoNi-CN_h 600/G; c) PdCoNi-CN_h 900/G; d) PdCoNi-CN_l 600/G; e) PdCoNi-CN_l 900/G. The experimental conditions are reported in the caption of Figure 4.

cies present in the system as the ORR takes place. With respect to oxygen atoms, the adsorption energy (AE) of chlorine atoms both on Pd and Pt low-index surfaces is significantly lower.^[43] However, the difference between the AEs of oxygen and chlorine atoms is significantly lower for Pd than for Pt. Thus, with respect to the Pt/C reference, chloride anions can probably displace oxygen species from the surface of the PdCoNi-CN_x T_f/G electrocatalysts more easily. It is hypothesized that, with respect to the Pt/C reference, at a given concentration of chloride anions in the bulk electrolyte, the surface concentration of chlorine-based species on the active sites in alloy NPs of PdCoNi-CN_x T_f/G electrocatalysts is larger, giving rise to a decreased density of couples of neighboring active sites free of contaminants.^[11] As a result, with respect to the Pt/C reference, the ORR kinetics of the PdCoNi-CN_l T_f/G electrocatalysts and the selectivity in the four-electron mechanism are inferior, in accordance with previous reports on the effects of chloride contamination in the ORR carried out on PGM surfaces,^[15] and with the results shown in Figure 7 and Figure 9. The degradation of both ORR kinetics and ORR selectivity in the four-electron mechanism in the presence of Cl^- anions is likely mitigat-

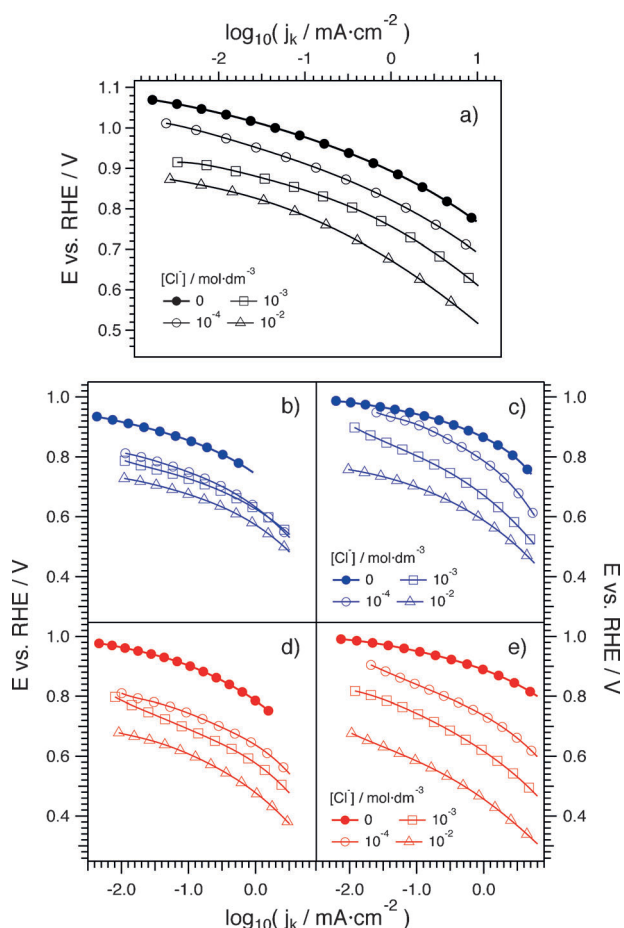


Figure 8. Tafel plots in a pure-oxygen atmosphere at increasing $[Cl^-]$ obtained from the rotating ring-disk traces displayed in the Supporting Information. a) Pt/C reference; b) PdCoNi-CN_h 600/G; c) PdCoNi-CN_h 900/G; d) PdCoNi-CN 600/G; e) PdCoNi-CN 900/G. The experimental conditions are reported in the caption of Figure 4.

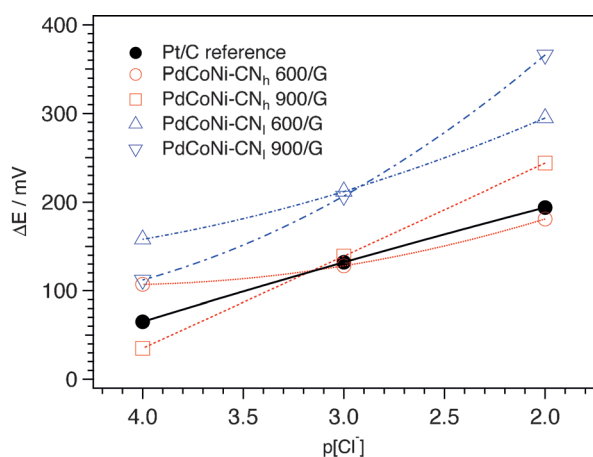


Figure 9. Potential shift of the Tafel plots as a function of the $[Cl^-]$. Differences from the traces corresponding to $[Cl^-]=0$ reported in Figure 8. Values determined at $\log_{10}(\text{Current Density}) = -1$.

ed by coordination of alloy NPs by N-based ligands forming coordination nests in the CN “shell” matrix. This effect is more pronounced for the PdCoNi-CN_h T_f/G electrocatalysts, which in-

clude a larger wt% of N atoms in comparison with PdCoNi-CN_l T_f/G materials. Indeed, with respect to Pd-O, the Pd-N interactions are stronger, owing to the “soft” character of Pd,^[42] N-based coordination species of the matrix are likely not displaced by Cl^- anions. Thus, the presence of N-based ligands in the matrix impedes the adsorption of Cl^- anions on the active sites, owing to bifunctional and electronic effects on alloy NPs. In conclusion, the N-based ligands in the CN matrix reduce the density of Cl^- anions adsorbed on the surface of the Pd-alloy NPs of PdCoNi-CN_h T_f/G electrocatalysts, leading to lower ORR overpotentials and higher selectivity in the four-electron mechanism in comparison with PdCoNi-CN_l T_f/G systems. With respect to the PdCoNi-CN_l T_f/G electrocatalysts and the Pt/C reference, the surface concentration of Cl^- on alloy NPs of PdCoNi-CN_h T_f/G may also be decreased by the lower expected porosity of the carbon nitride “shell” (see Section 2.4). With respect to PdCoNi-CN_x 600/G electrocatalysts, in PdCoNi-CN_x 900/G materials the increase in the ORR overpotential as $[Cl^-]$ is raised is larger (see Figure 9). This result is attributed to a decreasing overall concentration of adsorbates on the alloy NPs as T_f is raised. The Tafel slope values, as shown in Table S6 of the Supporting Information, increase in the order: Pt/C reference < PdCoNi-CN_x 600/G < PdCoNi-CN_x 900/G. In general, $[Cl^-]$ affects the Tafel slope values very little for each electrocatalyst. However, a significant increase is observed for PdCoNi-CN_x 900/G as $[Cl^-]$ is raised from 0 to 10^{-4} mol·dm⁻³. The curvature of ORR Tafel plots of the Pt/C reference in the presence of increasing $[Cl^-]$ anions does not change significantly, as shown in Figure 8a. Thus, the ORR rate-determining step is not expected to change, as reported elsewhere for similar systems.^[11] The same trends were also observed for PdCoNi-CN_x T_f/G electrocatalysts, with the exception of PdCoNi-CN_x 900/G as $[Cl^-]$ is raised from 0 to 10^{-4} M (see Figure 8c and e). This result is interpreted as indicating that on both Pt- and Pd-based systems, the effect of chloride anions in the ORR is mainly manifested by blocking of active sites, as evidenced in the discussion above and elsewhere.^[11,52] The Tafel slope values increase as each chloride anion is better able to displace oxygen-based species from the active sites of alloy NPs. The resulting surface has a lower concentration of oxygen-based adsorbates, which are known to reduce the ORR Tafel slope values.^[6] In this respect, the displacement: 1) is easiest on the active sites of alloy NPs of PdCoNi-CN_x 900/G electrocatalysts, which are relatively free of adsorbates; 2) is more difficult on PdCoNi-CN_x 600/G, for which the concentration of adsorbates is significant; and 3) is hardest on the Pt-based surfaces of the Pt/C reference. The significant increase in ORR Tafel slope values observed for PdCoNi-CN_x 900 electrocatalysts as $[Cl^-]$ is raised from 0 to 10^{-4} mol·dm⁻³ is attributed to the deactivation of the bifunctional mechanism owing to the increased ORR overpotential in the presence of Cl^- contamination.

3. Conclusions

Four PdCoNi “core-shell” carbon nitride electrocatalysts with the general formula PdCoNi-CN_x T_f/G have been prepared. A detailed powder XRD, morphological, and electrochemical

study has been carried out, with the purpose of elucidating the complex interplay between the chemical composition, morphology, structure, and performance of the PdCoNi-CN_x T_f/G electrocatalysts in the ORR. The results allow us to conclude that the most relevant features are: 1) the phase parameters of the PdCoNi alloy NPs bearing the active ORR sites, with a particular reference to the cell constant and the grain size; and 2) the details of the interactions taking place between the carbon nitride “shell” matrix and the PdCoNi alloy NPs. It is shown that the best ORR performance is obtained when the cell constant of the PdCoNi alloy NPs is shortest and when a low concentration of N is included in the carbon nitride “shell” of the materials. In detail, as T_f is raised to 900 °C, the alloying degree of the PdCoNi alloy NPs increases, yielding a contraction of the cell constant, which promotes the ORR kinetics by means of an electronic effect.^[35] A high alloying degree is also expected to give rise to an additional improvement of ORR kinetics by means of a bifunctional mechanism involving neighboring Pd and Co/Ni atoms on the surface of alloy NPs.^[21] Furthermore, the N-based ligands forming the “coordination nests” in the carbon nitride “shell” are good binding sites for alloy NPs, consequently modulating the performance of PdCoNi ORR active sites. However, it is highlighted that N-based ligands in the matrix play an important and beneficial role because they hinder the growth of the PdCoNi alloy NPs, leading to smaller grain sizes, and because they improve the tolerance of the electrocatalysts to chloride anion contamination. PdCoNi-CN₁ 900/G shows the best ORR performance because it includes PdCoNi NPs with a high alloying degree, which yield a very good ORR performance owing to the combination of both the electronic and the bifunctional mechanisms, and because it has a porous carbon nitride “shell” with a low concentration of N, which stabilizes PdCoNi ORR active sites in alloy NPs and improves the conductivity of the CN matrix. As a result, with respect to the Pt/C reference, the surface activity at 0.9 V vs. RHE of the PdCoNi-CN₁ 900/G electrocatalyst in the ORR is significantly higher (388 μA cm_{Pd}⁻² vs. 153 μA cm_{Pt}⁻²).

In summary, the proposed PdCoNi-CN_x T_f/G systems are very promising materials for further optimization in the search for improved ORR electrocatalysts for application at the cathode of PEMFCs.

Experimental Section

Reagents and Preparation of the Electrocatalysts

The PdCoNi-CN_h T_f/G electrocatalysts were prepared according to a general procedure described elsewhere.^[21] Details of the preparation of the PdCoNi-CN_x 900/G electrocatalysts were reported in a previous publication.^[47] PdCoNi-CN_x 600/G systems were obtained according to the same protocol, with the difference that the final pyrolysis process was carried out for 2 h at T_f = 600 °C instead of T_f = 900 °C. EC-20 was obtained from ElectroChem, Inc. (nominal Pt loading: 20%) and used as a reference electrocatalyst (“Pt/C reference”). Vulcan XC-72R carbon black, provided as a courtesy by Carbocrom s.r.l., was treated with H₂O₂ 10 vol% prior to use.

Instruments and Methods

The wt% of the metals in the PdCoNi-CN_x T_f/G electrocatalysts was determined by ICP-AES analysis by using the method of standard additions. The emission lines used were: λ = 340.458 (Pd), 228.616 (Co), 231.604 (Ni), and 766.490 nm (K). Details of the ICP-AES spectrometer and sample mineralization procedure are reported elsewhere.^[41] The wt% of carbon and nitrogen in each sample were determined by elemental analysis, which was carried out with a FISON EA-1108 CHNS-O instrument. XRD measurements were collected with a Philips X'Pert instrument with a vertical goniometer and a Bragg–Brentano geometry, adopting a highly stabilized generator. The instrument was equipped with a focusing graphite monochromator and a proportional counter with a pulse-height discriminator. Spectra were collected with a stepwise technique (2θ steps of 0.05°, collection time equal to 10 s-step⁻¹). The semi-quantitative phase analysis was carried out by using the Rietveld method with the MAUD program.^[30] Morphology studies carried out with HR-TEM were executed with sample preparation techniques and experimental setup described elsewhere.^[53] The samples were suspended in isopropyl alcohol, and a drop (5 μL) was deposited on a holey carbon film supported on a 3 mm copper grid. Images were collected with a Jeol 3010 microscope operating at 300 kV. The instrument was fitted with a Gatan slowscan 794 CCD camera. Porous electrodes were prepared according to a procedure described elsewhere.^[53] Each electrocatalyst was diluted with XC-72R in a 1:1 weight ratio, and the resulting mixture was ground extensively by hand in an agate mortar; no XC-72R was added to the Pt/C reference. Catalyst inks were prepared by adding suitable amounts of milli-Q water and commercial Nafion solution (Alfa Aesar, 5% weight) to these powders. 15 μL of each ink were then transferred to the top of a freshly-polished glassy carbon electrode tip with a geometrical area (A) equal to 0.196 cm², yielding an overall loading of Pd or Pt equal to approximately 15 μg cm⁻². Further details on the electrochemical setup are reported elsewhere.^[41] An Hg/HgSO₄/K₂SO₄(sat.) reference electrode was adopted for the experiments. All the potentials are expressed in terms of the reversible hydrogen electrode (RHE) scale, calibrated by H₂ oxidation/reduction measurements on a platinized platinum electrode. The experiments were carried out using 0.1 M HClO₄ solution as the electrolyte at a temperature of 60 °C. High-purity nitrogen, oxygen, and carbon monoxide (Air Liquide) were used to saturate the electrochemical cell and to investigate the electrochemical features of the materials. Details of the activation and CO stripping measurements carried out on the electrocatalysts are reported elsewhere.^[41] The ORR performance of the materials was evaluated by collecting linear sweep voltammograms (LSVs) from 0.135 to 1.24 V vs. RHE at 5 mV s⁻¹. The poisoning effect of chloride anions in the ORR was evaluated as described elsewhere by collecting LSVs at 5 mV s⁻¹ at increasing chloride anion concentrations of 0, 10⁻⁴, 10⁻³, and 10⁻² mol dm⁻³.^[24]

Acknowledgements

This research was funded by the strategic project of the University of Padova “MAESTRA” - From Materials for Membrane-Electrode Assemblies to Electric Energy Conversion and Storage Devices. K.V. thanks Veneto Nanotech S.C.p.a. for financial support.

Keywords: electrocatalysis • fuel cells • nanoparticles • oxygen reduction reaction • X-ray diffraction

- [1] Z. Yang, J. Zhang, M. C. W. Kintner-Meyer, X. Lu, D. Choi, J. P. Lemmon, J. Liu, *Chem. Rev.* **2011**, *111*, 3577–3613.
- [2] G. A. Snook, P. Kao, A. S. Best, *J. Power Sources* **2011**, *196*, 1–12.
- [3] K. D. Kreuer, *Chem. Mater.* **2014**, *26*, 361–380.
- [4] R. O'Hayre, S. W. Cha, W. Colella, F. B. Prinz, *Fuel Cell Fundamentals*, John Wiley & Sons, Hoboken, NJ **2006**.
- [5] Y. Wang, K. S. Chen, J. Mishler, S. C. Cho, X. C. Adroher, *Appl. Energy* **2011**, *88*, 981–1007.
- [6] J. X. Wang, F. A. Uribe, T. E. Springer, J. Zhang, R. R. Adzic, *Faraday Discuss.* **2009**, *140*, 347–362.
- [7] J. Zhang, *Front. Energy* **2011**, *5*, 137–148.
- [8] Z. Chen, D. Higgins, A. Yu, L. Zhang, J. Zhang, *Energy Environ. Sci.* **2011**, *4*, 3167–3192.
- [9] A. J. Appleby, *Sci. Am.* **1999**, *281*, 74–79.
- [10] R. L. Moss, E. Tzimas, P. Willis, J. Arendorf, L. Tercero-Espinoza, *Critical Metals in the Path towards the Decarbonisation of the EU Energy Sector - Assessing Rare Metals as Supply-Chain Bottlenecks in Low-Carbon Energy Technologies*, Publications Office of the European Union, Luxembourg **2013**.
- [11] T. J. Schmidt, U. A. Paulus, H. A. Gasteiger, R. J. Behm, *J. Electroanal. Chem.* **2001**, *508*, 41–47.
- [12] R. Borup, J. Meyers, B. Pivovar, Y. S. Kim, R. Mukundan, N. Garland, D. Myers, M. Wilson, F. Garzon, D. Wood, P. Zelenay, K. More, K. Stroh, T. A. Zawodzinski, J. Boncella, J. E. McGrath, M. Inaba, K. Miyatake, M. Hori, K. Ota, Z. Ogumi, S. Miyata, A. Nishikata, Z. Siroma, Y. Uchimoto, K. Yasuda, K. Kimijima, N. Iwashita, *Chem. Rev.* **2007**, *107*, 3904–3951.
- [13] K. A. Jaaf-Golze, D. M. Kolb, D. Scherson, *J. Electroanal. Chem. Interfacial Electrochem.* **1986**, *200*, 353–362.
- [14] B. Pozniak, Y. Mo, D. A. Scherson, *Faraday Discuss.* **2002**, *121*, 313–322.
- [15] V. Stamenkovic, N. M. Markovic, P. N. J. Ross, *J. Electroanal. Chem.* **2001**, *500*, 44–51.
- [16] M. Arenz, V. Stamenkovic, T. J. Schmidt, K. Wandelt, P. N. Ross, N. M. Markovic, *Surf. Sci.* **2003**, *523*, 199–209.
- [17] E. Antolini, *Energy Environ. Sci.* **2009**, *2*, 915–931.
- [18] E. Antolini, T. Lopes, E. R. Gonzalez, *J. Alloys Compd.* **2008**, *461*, 253–262.
- [19] M. H. Shao, *J. Power Sources* **2011**, *196*, 2433–2444.
- [20] V. Di Noto, E. Negro, S. Polizzi, P. Riello, P. Atanassov, *Appl. Catal. B* **2012**, *111–112*, 185–199.
- [21] V. Di Noto, E. Negro, *Electrochim. Acta* **2010**, *55*, 7564–7574.
- [22] V. Di Noto, E. Negro, US Patent PCT/IT2009/000278, **2009**.
- [23] V. Di Noto, E. Negro, S. Polizzi, F. Agresti, G. A. Giffin, *ChemSusChem* **2012**, *5*, 2451–2459.
- [24] V. Di Noto, E. Negro, K. Vezzù, L. Toniolo, G. Pace, *Electrochim. Acta* **2011**, *57*, 257–269.
- [25] E. Negro, S. Polizzi, K. Vezzù, L. Toniolo, G. Cavinato, V. Di Noto, *Int. J. Hydrogen Energy* **2014**, *39*, 2828–2841.
- [26] V. Di Noto, E. Negro, S. Polizzi, K. Vezzù, L. Toniolo, G. Cavinato, *Int. J. Hydrogen Energy* **2014**, *39*, 2812–2827.
- [27] S. Chumillas, C. Busó-Rogero, J. Solla-Gullón, F. J. Vidal-Iglesias, E. Herrero, J. M. Feliu, *Electrochem. Commun.* **2011**, *13*, 1194–1197.
- [28] A. López-Cudero, J. Solla-Gullón, E. Herrero, A. Aldaz, J. M. Feliu, *J. Electroanal. Chem.* **2010**, *644*, 117–126.
- [29] V. Mazumder, Y. Lee, S. Sun, *Adv. Funct. Mater.* **2010**, *20*, 1224–1231.
- [30] L. Lutterotti, Maud—Materials Analysis Using Diffraction. **2010**, ver. 2.33, <http://www.ing.unitn.it/~maud/>.
- [31] L. Zhang, K. Lee, J. Zhang, *Electrochim. Acta* **2007**, *52*, 3088–3094.
- [32] L. Chen, H. Guo, T. Fujita, A. Hirata, W. Zhang, A. Inoue, M. Chen, *Adv. Funct. Mater.* **2011**, *21*, 4364–4370.
- [33] JCPDS-ICDD, PCPDFWIN Database. **2000**, Version 2.1.
- [34] L. Zhang, L. Wan, Y. Ma, Y. Chen, Y. Zhou, Y. Tang, T. Lu, *Appl. Catal. B* **2013**, *138–139*, 229–235.
- [35] M. H. Shao, K. Sasaki, R. R. Adzic, *J. Am. Chem. Soc.* **2006**, *128*, 3526–3527.
- [36] H. Berg, J. B. Cohen, *Metall. Trans.* **1972**, *3*, 1797–1805.
- [37] V. Di Noto, E. Negro, R. Gliubizzi, S. Gross, C. Maccato, G. Pace, *J. Electrochem. Soc.* **2007**, *154*, B745–B756.
- [38] M. T. M. Koper, S. C. S. Lai, E. Herrero in *Fuel Cell Catalysis - A surface science approach* (Ed.: M. T. M. Koper), John Wiley & Sons, Hoboken, NJ **2009**, pp. 159–208.
- [39] A. Pozio, M. De Francesco, A. Cemmi, F. Cardellini, L. Giorgi, *J. Power Sources* **2002**, *105*, 13–19.
- [40] F. C. Nart, W. Vielstich, in *Handbook of Fuel Cells: Fundamentals Technology and Applications, Vol. 1* (Eds.: W. Vielstich, A. Lamm, H. A. Gasteiger), John Wiley & Sons, Chichester, **2003**, pp. 302–315.
- [41] V. Di Noto, E. Negro, *Fuel Cells* **2010**, *10*, 234–244.
- [42] F. Basolo, R. J. Pearson, *Mechanisms of Inorganic Reactions*, John Wiley & Sons, New York **1967**.
- [43] L. Xiao, L. Zhuang, Y. Liu, J. Lu, H. D. Abruña, *J. Am. Chem. Soc.* **2009**, *131*, 602–608.
- [44] B. Beden, S. Bilmes, C. Lamy, J. M. Leger, *J. Electroanal. Chem.* **1983**, *149*, 295–302.
- [45] H. Yang, N. Alonso-Vante, J. M. Léger, C. Lamy, *J. Phys. Chem. B* **2004**, *108*, 1938–1947.
- [46] H. A. Gasteiger, S. S. Kocha, B. Sompalli, F. T. Wagner, *Appl. Catal. B-Environ.* **2005**, *56*, 9–35.
- [47] V. Di Noto, E. Negro, S. Lavina, N. Boaretto, M. Piga, *ECS Trans.* **2008**, *16*, 123–137.
- [48] M. Gattrell, B. MacDougall, in *Handbook of Fuel Cells: Fundamentals Technology and Applications, Vol. 1* (Eds.: W. Vielstich, A. Lamm, H. A. Gasteiger), John Wiley & Sons, Chichester, **2003**, pp. 443–464.
- [49] G. Wu, P. Zelenay, *Acc. Chem. Res.* **2013**, *46*, 1878–1889.
- [50] W. M. Wang, D. Zheng, C. Du, Z. Q. Zou, X. G. Zhang, B. J. Xia, H. Yang, D. L. Akins, *J. Power Sources* **2007**, *167*, 243–249.
- [51] T. J. Schmidt, H. A. Gasteiger in *Handbook of Fuel Cells: Fundamentals Technology and Applications, Vol. 2* (Eds.: W. Vielstich, A. Lamm, H. A. Gasteiger), John Wiley & Sons, Chichester, **2003**, pp. 316–333.
- [52] U. A. Paulus, T. J. Schmidt, H. A. Gasteiger in *Handbook of Fuel Cells: Fundamentals Technology and Applications, Vol. 2* (Eds.: W. Vielstich, A. Lamm, H. A. Gasteiger), John Wiley & Sons, Chichester, **2003**, pp. 555–569.
- [53] V. Di Noto, E. Negro, R. Gliubizzi, S. Lavina, G. Pace, S. Gross, C. Maccato, *Adv. Funct. Mater.* **2007**, *17*, 3626–3638.

Received: March 8, 2014

Revised: June 2, 2014

Published online on August 5, 2014